ADVANCED SCIENCE NEWS
www.advancedsciencenews.com

Tin Sulfide-Based Nanohybrid for High-Performance Anode of Sodium-Ion Batteries

Jaewon Choi, Na Rae Kim, Kyungmi Lim, Kyojin Ku, Hyeon Ji Yoon, Jin Gu Kang, Kisuk Kang, Paul V. Braun, Hyoung-Joon Jin, and Young Soo Yun**

***N**anohybrid anode materials for Na-ion batteries (NIBs) based on conversion and/or alloying reactions can provide significantly improved energy and power characteristics, while suffering from low Coulombic efficiency and unfavorable voltage properties. An NIB paper-type nanohybrid anode (PNA) based on tin sulfide nanoparticles and acid-treated multiwalled carbon nanotubes is reported. In 1 M $NaPF_6$ dissolved in diethylene glycol dimethyl ether as an electrolyte, the above PNA shows a high reversible capacity of ≈1200 mAh g^{-1} and a large voltage plateau corresponding to a capacity of ≈550 mAh g^{-1} in the low-voltage region of ≈0.1 V versus Na^+/Na, exhibiting high rate capabilities at a current rate of 1 A g^{-1} and good cycling performance over 250 cycles. In addition, the PNA exhibits a high first Coulombic efficiency of ≈90%, achieving values above 99% during subsequent cycles. Furthermore, the feasibility of PNA usage is demonstrated by full-cell tests with a reported cathode, which results in high specific energy and power values of ≈256 Wh kg^{-1} and 471 W kg^{-1}, respectively, with stable cycling.*

Dr. J. Choi, J. G. Kang, Prof. P. V. Braun
Department of Materials Science and Engineering
University of Illinois at Urbana-Champaign
Urbana, IL 61801, USA
Dr. J. Choi
Department of Chemistry
Sungkyunkwan University
Suwon 16419, South Korea
N. R. Kim, H. J. Yoon, Prof. H.-J. Jin
Department of Polymer Science and Engineering
Inha University
Incheon 402-751, South Korea
E-mail: hjjin@inha.ac.kr
K. Lim, K. Ku, Prof. K. Kang
Department of Materials Science and Engineering
Seoul National University
Seoul 151-742, South Korea
Prof. Y. S. Yun
Department of Chemical Engineering
Kangwon National University
Samcheok 245-711, South Korea
E-mail: ysyun@kangwon.ac.kr

DOI: 10.1002/smll.201700767

1. Introduction

Na-ion batteries (NIBs) have attracted much attention as a next-generation power source for portable mobile electronics, electric vehicles, and large-scale energy storage (grid energy storage) because of the wide availability, low cost, and abundance of Na.[1–4] The similarity of NIB chemistry to that of Li-ion batteries (LIBs), which are the major power sources in current electronic devices, enhances their near-future technological potential.[1–4] However, the unfavorable energy and power characteristics of NIBs compared to those of LIBs are critical issues to be resolved, originating from the intrinsic differences between Na and Li. The Na-ion is ≈55% larger and 330% heavier than the Li ion, exhibiting a 0.33 eV higher electropotential (vs elemental metal).[1–5] In addition, the commercial success of LIBs is partly due to the use of the graphite, which, however, exhibits poor Na-ion storage capacity. Thus, a more suitable anode material is required for NIBs, exhibiting a high capacity with a low-voltage plateau (<0.1 V vs Na^+/Na), high rate capability, and long-term cycling stability.[6] Hard carbons (disordered

graphitic carbons) were initially proposed as an anode material for NIBs, since they could deliver a reversible capacity of ≈300 mA h g^{-1} with a low-voltage plateau corresponding to ≈50% of the total capacity.[7–9] Nevertheless, the specific capacity is still lower than that of the conventional graphite-based LIB anode (≈372 mA h g^{-1}), and the rate capability and cycle lifetime are also insufficient. Although more advanced carbon-based anode materials have been recently developed through nanostructured design and tuning of the local carbon microstructure, the specific capacities and working voltages are still inferior to those of LIBs, moreover, these materials generally show a large irreversible capacity due to the large surface area that induces the formation of excess amount of solid-electrolyte interphase (SEI).[10–14] Therefore, various alternative anode materials based on metals/alloys,[15–20] metal oxides/sulfides/phosphides,[21–27] and organic materials[28–30] have been explored. Among them, tin sulfide (SnS) has a high theoretical capacity of ≈1020 mA h g^{-1}, with its charge storage mechanism featuring both the conversion reaction of sulfur and the alloying reaction of tin, described by Equations (1) and (2):[31–34]

$$SnS + 2Na^+ + 2e^- \leftrightarrow Na_2S + Sn \quad (1)$$

$$4Sn + 15Na^+ + 15e^- \leftrightarrow Na_{15}Sn_4 \quad (2)$$

Thus, 1 mol of SnS can store 5.75 mol of Na. The above reactions are accompanied by a large volume change during sodiation/desodiation, leading to poor cycling stability.[31–34] Therefore, a general strategy to improve the electrochemical performance of SnS features both downsizing it to nanometer-scale and producing nanohybrids with nanocarbon or coating a carbon layer on the surface of the nanostructured SnS.[31–38] Lu et al. reported SnS/reduced graphene oxide and/or hard carbon nanocomposites with a reversible capacity of ≈640 mA h g^{-1}, good rate capabilities at specific current rates from 50 to 500 mA g^{-1}, and stable behavior during 30 discharge/charge cycles.[32] In addition, Zhu et al. reported 3D porous interconnected SnS/carbon nanocomposites with a reversible capacity of ≈920 mA h g^{-1} and respectable rate and cycling performances.[33] While these reports demonstrate the potential merits of SnS-based nanohybrids as NIB anodes, it was found that the first Coulombic efficiencies and working voltages of these materials are not satisfactory. However, the SnS@graphene nanohybrids reported by Zhou et al. show a low-voltage plateau with a reversible capacity of ≈300 mA h g^{-1} at a low specific current rate (≈30 mA g^{-1}).[31] The authors claim that this plateau originates from the Sn–Na alloying reaction, which is supported by previous theoretical and experimental results.[34] Nevertheless, many reported Sn–Na alloying reactions show unfavorable voltage characteristics in their galvanostatic discharge/charge profiles for Na-ion storage.[15,16,25,32,33] The contradicting results are possibly due to the different electrochemical resistance of electrode materials. For the SnS@graphene nanohybrids, a low equivalent series resistance (ESR) of ≈50 Ω was observed, possibly caused by the graphene-based nanohybrid architecture.[31] However, these hybrids exhibit a low voltage plateau when a low specific current rate is applied, limiting their power characteristics. In addition, the high specific surface area of nanohybrid materials inevitably causes significant side reactions at the electrode/electrolyte interface, leading to low Coulombic efficiencies. Therefore, in order to achieve better-performing nanohybrid anode materials, their key parameters such as Coulombic efficiency and ESR should be improved.

In this study, we report a paper-type nanohybrid anode (PNA) based on SnS nanoparticles and acid-treated multiwalled carbon nanotubes (A-MWCNTs). Combined with the use of a new electrolyte system based on a linear-chain solvent, diethylene glycol dimethyl ether (DEGDME), instead of the conventional carbonate-based one, it is demonstrated that the PNAs show a first Coulombic efficiency of ≈90.0% and a large low-voltage plateau of ≈550 mA h g^{-1}, with a specific capacity of ≈410 mA h g^{-1} maintained even at a high specific current rate of 1 A g^{-1}. These energy and power characteristics surpass those of the conventional graphite-based LIB anode. Additionally, the PNAs are mechanically flexible, also exhibiting a potential advantage for enhanced volumetric and gravimetric energy densities due to the absence of the current collector, binder, and conducting carbon components. Moreover, the feasibility of PNAs was demonstrated by full-cell tests with a reported cathode, which showed high specific energy and power values of ≈256 Wh kg^{-1} and 471 W kg^{-1}, respectively.

2. Result and Discussion

Tetrahedral zinc blende (ZB) SnS nanocrystals were prepared via a colloidal synthetic route. Field-emission transmission electron microscopy (FE-TEM) images show that the SnS nanocrystals are ≈500 nm long on one side with a high crystallinity (**Figure 1**a,b). Most of the SnS nanocrystals have similar tetrahedral structures, with a narrow particle size distribution observed by field-emission scanning electron microscopy (FE-SEM) at low magnification (Figure 1c). Although the colloidal synthetic route can achieve a high SnS nanocrystal yield, carefully chosen synthetic conditions are required. The well-defined morphologies and crystal structure were obtained by controlling the Sn/S ratio, temperature, and reaction time (see Figure S1 in the Supporting Information). When the reaction temperature is higher than 230 °C, or the relative sulfur content compared to the Sn precursor content is greater than ≈10 mol%, an orthorhombic plate structure is favored over the ZB tetrahedron.[39] Half of the eight (111) faces of the tetrahedral structure have different surface free energies, affecting how the surfactant binds. Polarity could induce the formation of the tetrahedral ZB SnS nanocrystals.[39] Figure S2 (Supporting Information) displays characteristic X-ray diffraction (XRD) peaks of the tetrahedral ZB SnS structure, which include strong (111), (200), and (220) peaks at 26.5°, 30.7°, and 44.0°, respectively. MWCNTs with a high persistence length were acid-treated to achieve oxygen functionalization and purification. The morphologies of A-MWCNTs are shown in Figure 1d, exhibiting an interconnected network structure and a high aspect ratio above 100. The A-MWCNTs have a

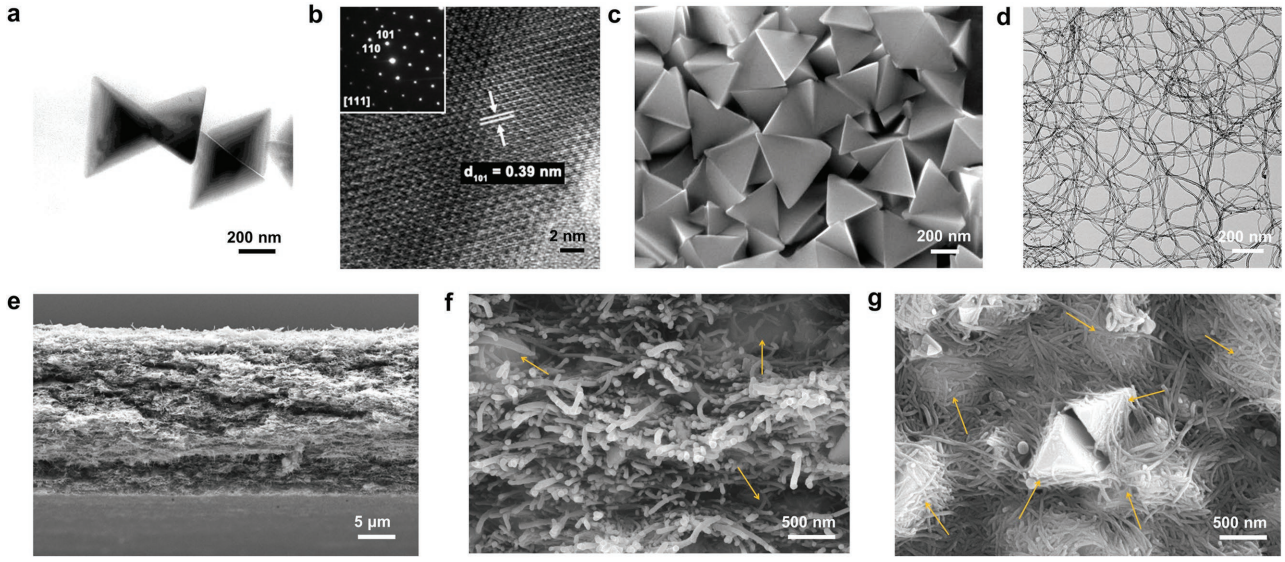

Figure 1. Morphological characterization of ZB SnS nanoparticles, A-MWCNTs, and PNAs. a) FE-TEM image and b) high-resolution FE-TEM image of ZB SnS nanoparticles (inset of selected area diffraction pattern). c) FE-SEM images of ZB SnS nanoparticles. d) FE-TEM image of A-MWCNTs. FE-SEM images of e,f) the fractured surface at different magnifications and g) the top surface of PNAs.

C/O ratio of 6.7, and their buckypapers have high electrical conductivities of ≈2.3×10^1 S cm^{-1}. Further specific information on A-MWCNTs can be found in Figure S3 (Supporting Information).

PNAs were prepared by simple vacuum filtration of the mixture of the prepared SnS nanoparticles and the A-MWCNTs dispersion. The thickness of A-MWCNTs and the corresponding SnS nanoparticle fraction are tunable by controlling the respective volumes and ratios. As shown in Figure 1e, PNAs of ≈25 μm thickness were prepared using a 0.05 wt% dimethylformamide (DMF) dispersion of solutes containing ≈60 wt% of SnS nanoparticles and ≈40 wt% of A-MWCNTs. The magnified fractured surface and top surface SEM images show that SnS nanoparticles were thoroughly bound by the A-MWCNT networks (Figure 1f,g). The weight ratios of SnS and the A-MWCNTs in the resulting PNAs were confirmed by thermogravimetric analysis (TGA) in air (Figure S4, Supporting Information). The TGA curve shows a residual weight of ≈60.3%, which is almost identical to the initial weight ratios of SnS and A-MWCNTs introduced during preparation. These results support the conclusion that the SnS nanoparticles are homogeneously dispersed in the A-MWCNT matrix; hence they show similar local weight ratios of around 60%. The XRD patterns of the PNAs show the characteristic peaks for both tetrahedral ZB SnS nanocrystals and A-MWCNTs (Figure S2, Supporting Information), indicating that their intrinsic structures are preserved in the physical mixture.

The electrochemical tests of PNAs were conducted by punching the paper (without any substrate, binder, and super P) in a 1 M $NaPF_6$ solution in DEGDME as an electrolyte. Cyclic voltammograms (CVs) of PNAs show several distinct peaks (**Figure 2**a). In the first cycle, a large cathodic peak centered at 0.84 V is observed, together with three oxidation and reduction peaks at 0.05/0.01, 0.19/0.20, and 0.69/0.63 V, indicating the occurrence of Na alloying/dealloying reactions.[34] Note that the low-voltage redox peak is markedly high in the intensity, indicating a well-defined low-voltage capacity. As shown in Figure S5 (Supporting Information), the low-voltage capacity do not originates from an Na metal plating reaction. In addition, the observed peak pair at 1.08/1.33 V is attributed to the conversion reaction with sulfur.[31] The Na-ion storage mechanism of PNAs was investigated in greater detail by ex situ XRD characterization at different states of charges (SoCs), as shown in **Figure 3**. The ex situ XRD patterns of PNAs sodiated at 1 and 0.7 V versus Na^+/Na show several initial SnS peaks disappearing and new Na_9Sn_4, Na_2S_5, and $Sn_{1-x}S$ peaks appearing at 0.7 V. This result indicates that the large cathodic peak at 0.84 V in the CV curve mainly originates from the structural change of SnS after Na-ion insertion, and not from the irreversible capacity due to the formation of a SEI layer. Upon discharge to 0.01 V versus Na^+/Na, the presence of $Na_{15}Sn_4$ was detected, revealing the full progress of the theoretical Sn–Na alloying reaction and supporting the CV result. Moreover, HNaS and Na_2S_2 peaks were detected, showing that the reaction was slightly deviated from the theoretically predicted one (Na_2S). The hydrogen atoms probably originate from A-MWCNTs, which could react with Na and S in a complex reaction. During the following charge to ≈0.4 V, the HNaS peak disappeared, suggesting a possible transformation to Na_2S_2. Additionally, the $Na_{15}Sn_4$ peak also disappeared, and several Sn metals and SnS peaks were detected. The dealloying of $Na_{15}Sn_4$ to Sn corresponds to the low-voltage plateau, and the presence of SnS peaks represents the reversible assembly of the initial SnS structure. Whereas similar SnS, Sn, and Na_2S_2 peaks were found at ≈1.4 V, no distinct peaks were detected after full charging to 2.7 V versus Na^+/Na, indicating that the reassembled SnS structure is amorphorized as the Na ions are extracted. Based on these CV data and ex situ XRD results, we can confirm that Sn and S mainly contribute to the reversible Na-ion storage by undergoing alloying and

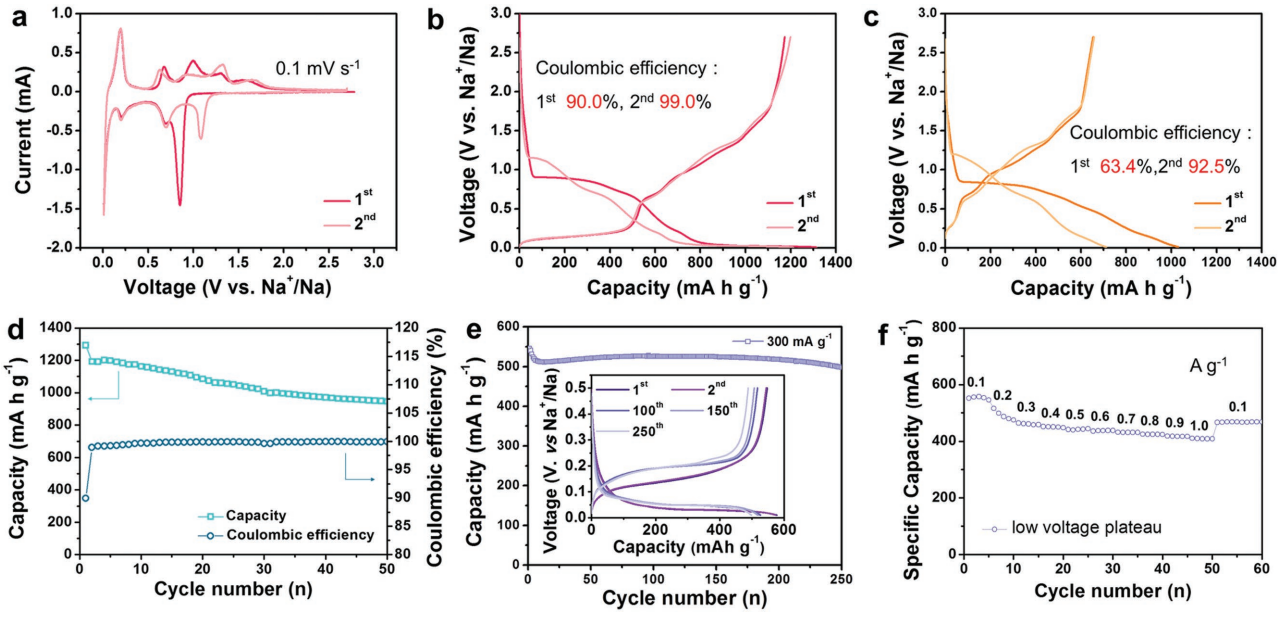

Figure 2. Electrochemical properties of PNAs. a) Cyclic voltammograms recorded at a sweep rate of 0.1 mV s^{-1} in a voltage window of 0.01–2.7 V versus Na^+/Na. Galvanostatic discharge/charge profiles in an electrolyte comprising 1 m $NaPF_6$ dissolved in b) DEGDME and c) EC/DEC (1:1 *v*/*v*) at a current rate of 300 mA g^{-1} in a voltage window of 0.01–2.7 V versus Na^+/Na. d) Cycling performance at a current rate of 300 mA g^{-1} during 50 cycles in a voltage window of 0.01–2.7 V versus Na^+/Na. e) Cycling performance at a current rate of 300 mA g^{-1} (Inset of galvanostatic discharge/charge profiles for 1st, 2nd, 100th, 150th and 250th cycles) and f) rate capabilities at different current rates of the low-voltage plateau in a voltage window of 0.01–0.5 V versus Na^+/Na.

conversion reactions, respectively. The galvanostatic discharge/charge profiles of PNAs show reversible Na-ion storage behavior with a high capacity of ≈1200 mA h g^{-1}, as shown in Figure 2b. Note that the Coulombic efficiency of the first cycle is ≈90.0%, despite the large electroactive surface area of the nanostructure based on SnS nanoparticles and A-MWCNTs. It implies that the first irreversible capacity originating from the electrolyte decomposition to form the SEI layer is relatively small, indicating that the DEGDME-based electrolyte is not significantly decomposed even at low voltages (below 1 V vs Na^+/Na). Moreover, the Coulombic efficiency reaches ≈99.0% in the following cycles, whereas the galvanostatic discharge/charge profiles of PNAs tested in a carbonate-based electrolyte (1 M $NaPF_6$ dissolved in ethylene carbonate (EC):diethylene carbonate (DEC) (1:1 *v*/*v*)) display relatively poor electrochemical performances. In this case, the reversible capacity is ≈655 mA h g^{-1}, the Coulombic efficiency being ≈63.4 and 92.5% for the first and second cycles, respectively. In particular, no low-voltage plateau is found in the carbonate-based electrolyte. This apparent discrepancy in the electrochemical performance was speculated to originate from the different solvents used and were further investigated by in situ electrochemical impedance spectroscopy (EIS) measurements for the first discharge/charge cycle, as shown in **Figure 4**. For the DEGDME system, exhibiting the first irreversible plateau at an early discharge stage, the EIS profiles show one large semicircle, corresponding to the charge transfer resistance (R_{ct}), as shown in Figure 4a. These semicircles become smaller with discharge time, and another small semicircle starts to form in their forepart. As a result, the initial large semicircle is deformed into an oval. Although the presence of the new semicircle is not clearly confirmed, the forepart of the oval-shaped semicircles could be attributed to the surface film resistance (R_f), which is generally caused by the formation of an insulating SEI layer and/or the deposition of decomposed electrolytes on the electrode surface. Small R_f values indicate the formation of a highly conductive and/or thin SEI layer. The ESR gradually decreased during the discharge process, reaching ≈13 Ω, which is a remarkably low value for the alloying/conversion reaction-based electrodes. In the following charge process, the low ESR value was maintained by an SoC of ≈10%, and finally one large semicircle was observed after the full extraction of Na ions (Figure 4b). Conversely, two large semicircles were found at the early discharge stage for the EC/DEC system, exhibiting a plateau (Figure 4c). The first and second

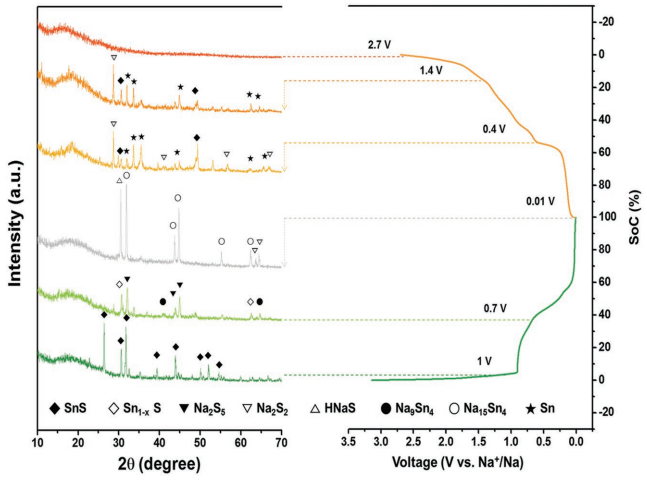

Figure 3. Ex situ XRD patterns of PNAs recorded at different SoCs.

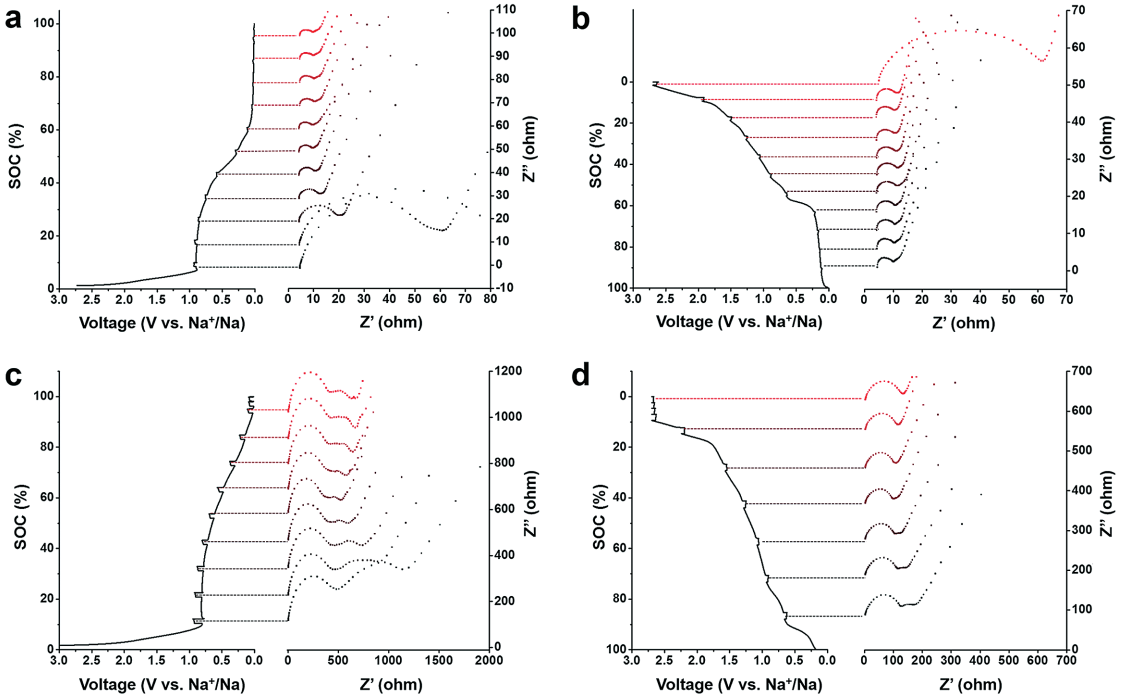

Figure 4. In situ EIS profiles of PNAs recorded at several intermittent rest times of the galvanostatic discharge/charge at a current rate of 300 mA g^{-1}: EIS profiles for a) discharge and b) charge in DEGDME. EIS profiles for c) discharge and d) charge in EC/DEC (1:1 *v*/*v*).

semicircles were attributed to R_f and R_{ct}, respectively. Whereas R_f showed similar values throughout the discharge process, R_{ct} changed according to the SoC. Note that R_f exceeds 400 Ω for all SoCs of the EC/DEC system, which could be related to the absence of the low-voltage plateau. The large polarization inevitably causes the overpotential during the discharge process, leading to an early voltage cut off before reaching the Na alloying reaction voltage. In the following charge process, the overall ESR values are considerably reduced, as shown in Figure 4d. Nevertheless, the ESR is still above ≈130 Ω, which is at least 10 times higher than that of the DEGDME system. Based on these EIS data, we conclude that the solvent system significantly affects the properties of the SEI layer formed in the first discharge process, inducing dramatic differences in electrochemical performance. These results agree with those of the CV measurements and galvanostatic discharge/charge profiles, as shown in Figure 2a–c. The cycling stabilities of PNAs were tested at a current rate of 0.3 A g^{-1}, as shown in Figure 2d. Although the initial capacity gradually decreased on cycling, a high value of ≈946 mA h g^{-1} was still maintained after 50 cycles. In addition, except for the first cycle, a Coulombic efficiency above 99% was achieved in all cycles without any additive. This superb cycling behavior contrasts with the cycling performance of the conventional SnS nanoparticle electrode system comprising an Al current collector, super P (20 wt%) and poly(vinylidene fluoride) (10 wt%) (Figure S6). The conventional SnS nanoparticle anode showed a dramatic capacity decrease, which was probably induced by the large volume expansion/contraction of SnS upon cycling.[40] However, ex situ SEM images of PNAs show that their thickness increased by ≈40 µm (60% of initial value) after full sodiation (Figures S7a,b, Supporting Information). In addition, after desodiation, the nanoparticle structure of SnS was re-established, although it was different from the original tetrahedral shape (Figures S7c,d, Supporting Information) and amorphous microstructure (Figure 3). This result suggests that the unique nanohybrid structure can effectively mitigate the volume change of SnS nanoparticles during sodiation/desodiation, inducing reversible Na-ion storage behavior. The cycling stabilities and rate capabilities of the low-voltage plateau of PNAs in the DEGDME-based electrolyte were further investigated in a voltage range between 0.01 and 0.5 V versus Na^+/Na (Figure 2e,f). The first reversible capacity of the low-voltage plateau equaled ≈550 mA h g^{-1} at a current rate of 300 mA g^{-1}, which is ≈1.5 times higher than the value of graphite (372 mA h g^{-1}) (Figure 2e). In a number of cycles, a sharp capacity drop of ≈50 mA h g^{-1} was observed, and a capacity of ≈500 mA h g^{-1} was retained after 250 cycles with a favorable voltage profile (average voltage of around 0.1 V vs Na^+/Na) (Inset, Figure 2e). This value is still higher than that of a typical graphite-based LIB anode. Ex situ FE-SEM images show that the paper-type morphologies of the PNAs were maintained after 250 cycles, although their thicknesses expanded by more than a factor of two and their internal microstructures were covered by reaction products and/or by-products (Figure S8, Supporting Information). These data suggest that the interconnected A-MWCNTs can provide conducting pathways, even under large volume expansions, while maintaining mechanical robustness in which their original paper-type morphologies are still maintained after long-term cycling. In addition, the low-voltage plateau exhibited notable rate capabilities and reversibility at current rates from 0.1 to 1.0 A g^{-1}, as shown in Figure 2f. Comparing with

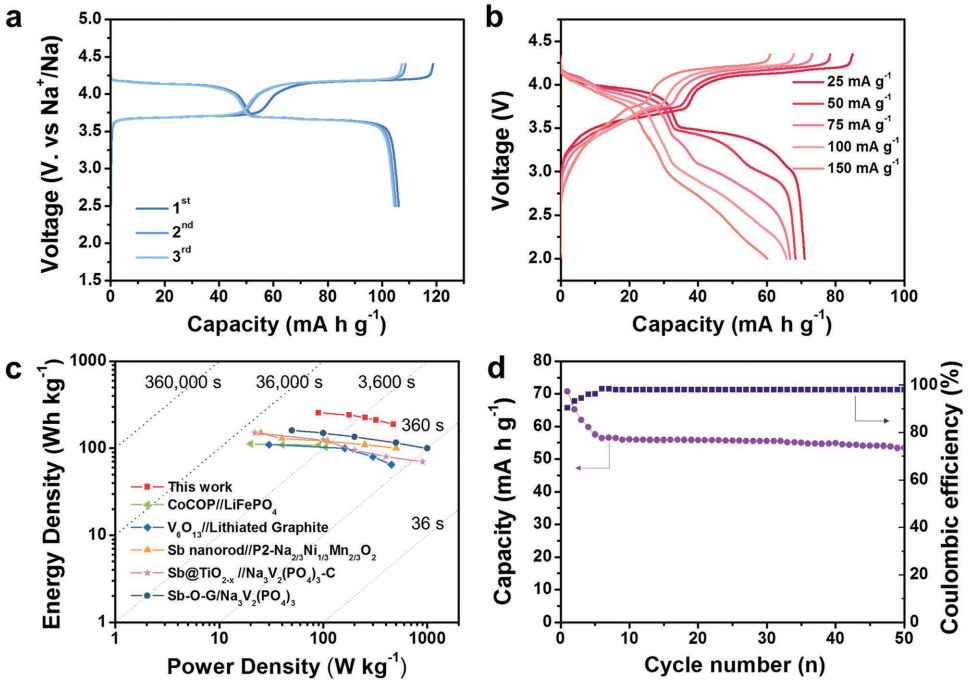

Figure 5. Electrochemical performances of PNA//$Na_{1.5}VPO_{4.8}F_{0.7}$ NIBs. a) Galvanostatic charge/discharge profiles of the $Na_{1.5}VPO_{4.8}F_{0.7}$ cathode at a current rate of 100 mA g^{-1} in a voltage window of 2.5–4.3 V versus Na^+/Na. b) Galvanostatic charge/discharge profiles of PNA//$Na_{1.5}VPO_{4.8}F_{0.7}$ NIBs at different current rates in a voltage window of 2.00–4.35 V. c) Ragone plots of several energy storage devices including PNA//$Na_{1.5}VPO_{4.8}F_{0.7}$, CoCOP//$LiFePO_4$,[37] V_6O_{13}//lithiated graphite,[38] Sb nanorod//P2-$Na_{2/3}Ni_{1/3}Mn_{2/3}O_2$,[39] Sb@$TiO_{2-x}$//$Na_3V_2(PO_4)_3$-C,[40] and Sb–O–G//$Na_3V_2(PO_4)_3$.[41] (d) Cycling performances at a current rate of 50 mA g^{-1} for 50 cycles.

the rate capability data characterized in a voltage range of 0.01–2.7 V versus Na^+/Na, the capacity drop of the low-voltage plateau with increasing current rate is insignificant, indicating the major capacity reduction is induced from the higher voltage section when the current rate is ranged from 0.1 to 1 A g^{-1} (Figure S9, Supporting Information). And the similar reversible capacities (≈1170 mA h g^{-1}) of PNAs were maintained, when the thickness of PNAs are much increased by ≈60 µm, as shown in Figure S10 (Supporting Information).

The feasibility of PNAs as a NIB anode was investigated by assembling full cells with a reported cathode material, $Na_{1.5}VPO_{4.8}F_{0.7}$.[41] The electrochemical performance of the cathode was first tested in a voltage range between 2.5 and 4.4 V versus Na^+/Na, using 1 M $NaPF_6$ dissolved in DEGDME as an electrolyte, as shown in **Figure 5**a. The galvanostatic charge/discharge profiles of the $Na_{1.5}VPO_{4.8}F_{0.7}$ cathode agreed with the previously reported ones,[41] showing a reversible capacity of ≈106 mA h g^{-1} at a current rate of 100 mA g^{-1}. The specific design of the full cells is schematically depicted in Figure S11 (Supporting Information). To assemble the full cells, PNAs were pre-cycled as half cells with Na metal in a voltage range between 0.01 and 0.5 V versus Na^+/Na for 10 cycles, and the open-circuit-voltage of PNAs was tuned to 0.5 V versus Na^+/Na in order to mainly utilize the low-voltage plateau (Figure S11, Supporting Information). Figure 5b shows the galvanostatic charge/discharge profiles of PNA//$Na_{1.5}VPO_{4.8}F_{0.7}$ NIBs at different current rates between 2.0 and 4.35 V. At a current rate of 25 mA g^{-1}, an average voltage of 3.6 V and a reversible capacity of 71.0 mA h g^{-1} were achieved, corresponding to a specific energy and power of ≈256 Wh kg^{-1} and ≈90 W kg^{-1}, respectively. As the current rates increased to 50, 75, 100, and 150 mA g^{-1}, the average voltages and capacities gradually decreased, resulting in the reduction of specific energy to ≈241, ≈225, ≈211, and ≈189 Wh kg^{-1}, respectively, while the respective specific powers record ≈176, ≈253, ≈321, and ≈471 W kg^{-1} (Table S1, Supporting Information). The Ragone plot of PNA//$Na_{1.5}VPO_{4.8}F_{0.7}$ NIBs shows the relationship of their energy and power characteristics more clearly, as depicted in Figure 5c. Worthwhile to note is that the specific energy of PNA//$Na_{1.5}VPO_{4.8}F_{0.7}$ is superior to the ones observed for previously reported systems such as CoCOP//$LiFePO_4$,[42] V_6O_{13}//lithiated graphite,[43] Sb nanorod//P2-$Na_{2/3}Ni_{1/3}Mn_{2/3}O_2$,[44] Sb@$TiO_{2-x}$//$Na_3V_2(PO_4)_3$-C,[45] and Sb–O–G/$Na_3V_2(PO_4)_3$,[46] demonstrating the practicability of PNA-based NIBs as an alternative to LIBs. Moreover, the PNA//$Na_{1.5}VPO_{4.8}F_{0.7}$ NIBs showed stable cycling performances over 50 consecutive cycles, displaying an ≈75% capacity retention (Figure 5d).

3. Conclusion

In conclusion, highly crystalline ZB SnS nanoparticles with ≈500 nm lengths and homogeneous size distributions were fabricated using a colloidal synthetic route featuring a controlled Sn/S ratio, reaction time, and temperature and combined with A-MWCNTs with a high aspect ratio to yield the mechanically flexible composite electrode for NIBs. In 1 M $NaPF_6$ dissolved in DEGDME as an electrolyte, these

PNAs showed a high reversible capacity of ≈1200 mA h g^{-1} and a high Coulombic efficiency of ≈90% in the first cycle. In addition, PNAs exhibited a significantly large plateau corresponding to a capacity of ≈550 mA h g^{-1} in the low-voltage area of ≈0.1 V versus Na^+/Na, showing high rate capabilities, good reversibility, and stable cycling performance over 250 cycles. Ex situ XRD patterns of PNAs at different SoCs revealed that the low-voltage plateau originates from the reversible formation of $Na_{15}Sn_4$ in Sn–Na alloying reactions along with the conversion reaction between S with Na ions contributing to the specific capacity. The results of in situ EIS revealed that PNAs show much lower R_f and ESR values (13 Ω) in DEGDME than in conventional carbonate-based solvents. The small R_f and high first Coulombic efficiency could account for the low-voltage plateau in DEGDME electrolyte system. The feasibility of PNA application was confirmed by tests of full cells assembled using a reported cathode, $Na_{1.5}VPO_{4.8}F_{0.7}$. The PNA//$Na_{1.5}VPO_{4.8}F_{0.7}$ NIBs showed a specific energy and power of ≈256 Wh kg^{-1} and ≈471 W kg^{-1}, respectively, with stable cycling.

4. Experimental Section

Fabrication of SnS Nanoparticles and A-MWCNTs: A 50 mL two-neck Schlenk flask was charged with oleylamine (10 mL) and vacuum-dried at 110 °C for 3 h, followed by the addition of sulfur (18 mg, 0.56 mmol) under argon. After 10 min of stirring, the flask was air-cooled to room temperature. $SnCl_2$ (100 mg, 0.53 mmol) was vacuum-dried for 10 min and dissolved in the above mixture. The reaction flask was heated to 230 °C and held for 2 h under Ar atmosphere. After the reaction, the resulting products were several times washed with ethanol and centrifuged. The obtained SnS nanoparticles were dried and stored in a vacuum oven at 30 °C. Pristine MWCNTs (CM-280, Hanhwa Chemical Co., Ltd., Seoul, Korea) were treated by a mixture of acids (sulfuric acid:nitric acid = 3:1 *v*/*v*) at 60 °C for 6 h to remove impurities and introduce surface oxygen functional groups. The obtained A-MWCNTs were neutralized by repetitive filtration and washing with distilled water. Finally, the A-MWCNTs were dried and stored in a vacuum oven at 30 °C.

Preparation of PNAs: SnS nanoparticles (21 mg) and A-MWCNTs (14 mg) were dispersed in DMF (70 g, 99.5%, Sigma-Aldrich, USA) by ultrasonication. The obtained mixture was filtered on an Anodisc membrane filter (47 mm diameter, 0.2 µm pores; Whatman). After drying in a convection oven at 80 °C, the obtained PNAs were separated from the filter and heated at 300 °C for 2 h.

Material Characterization: Sample morphologies were characterized using FE-SEM (S-4300, Hitachi, Japan) and FE-TEM (JEM2100F, JEOL, Japan). Chemical states were investigated by X-ray photoelectron spectroscopy (PHI 5700 ESCA) using monochromated Al Kα radiation ($h\nu$ = 1486.6 eV). Raman spectra were recorded using a continuous-wave linearly polarized laser (wavelength: 514.5 nm; energy: 2.41 eV; power: 16 mW). XRD (Rigaku DMAX 2500) was performed using Cu Kα radiation (λ = 0.154 nm), and the instrument was operated at 40 kV and 100 mA. Sample porosity was analyzed based on nitrogen adsorption and desorption isotherms obtained at –196 °C using a surface area and porosimetry analyzer (ASAP 2020, Micromeritics, USA).

Electrochemical Characterization: Electrochemical tests of PNAs, $Na_{1.5}VPO_{4.8}F_{0.7}$, and the corresponding full-cell devices were conducted using a WonATech automatic battery cycler and CR2032-type coin cells. In situ EIS tests were performed at room temperature in the frequency range of 1 MHz to 1 mHz using an impedance analyzer (ZIVE SP2, WonATech). The working electrodes were prepared by punching PNAs into circles with a diameter of 1/2 inch and an area density of ≈2.2 mg cm^{-2}. The SnS nanoparticle-based electrode and the $Na_{1.5}VPO_{4.8}F_{0.7}$ cathode were prepared by mixing the active material (SnS nanoparticles, 70 wt%) with conductive carbon (20 wt%) and PVDF (10 wt%) in *N*-methyl-2-pyrrolidone. The resulting slurries were uniformly applied onto Al foil. The electrodes were dried at 120 °C for 2 h and roll-pressed. The coin cells were assembled in a glove box filled with argon, employing a composite electrode with metallic sodium foil and 1 M $NaPF_6$ (Aldrich, purity: 98%) in DEGDME or EC/DEC (1:1 *v*/*v*) as the electrolyte. A glass microfiber filter (GF/F, Whatman) was used as a separator. The cells were galvanostatically cycled between 0.01 and 2.7 V versus Na^+/Na for half-cells and between 2.0 and 4.35 V for full cells at various current densities. For the full-cell assembly, PNAs were precycled as half-cells with Na metal in a voltage range of 0.01–0.5 V versus Na^+/Na for 10 cycles, and $Na_{1.5}VPO_{4.8}F_{0.7}$ was used in a fivefold weight excess to PNA.

Supporting Information

Supporting Information is available from Wiley Online Library or from the author.

Acknowledgements

J.C. and N.R.K. contributed equally to this work. This work was supported by the Industrial Strategic Technology Development Program (Project No. 10050477, Development of a separator with low thermal shrinkage and electrolyte with high ionic conductivity for Na-ion batteries) and was funded by the Ministry of Trade, Industry and Energy. This research was also supported by Basic Science Research Program through the National Research Foundation of Korea (NRF) funded by the Ministry of Education (NRF-2016R1A2B4009601), (2016R1A6A3A11930304) and (No. 2017R1C1B1004167).

Conflict of Interest

The authors declare no conflict of interest.

[1] N. Yabuuchi, M. Kajiyama, J. Iwatate, H. Nishikawa, S. Hitomi, R. Okuyama, R. Usui, Y. Yamada, S. Komaba, *Nat. Mater.* **2012**, *11*, 512.
[2] S. I. Park, I. Gocheva, S. Okada, J.-I. Yamaki, *J. Electrochem. Soc.* **2011**, *158*, A1067.
[3] S. P. Ong, V. L. Chevrier, G. Hautier, A. Jain, C. Moore, S. Kim, X. Ma, G. Ceder, *Energy Environ. Sci.* **2011**, *4*, 3680.

[4] Y. Cao, L. Xiao, M. L. Sushko, W. Wang, B. Schwenzer, J. Xiao, Z. Nie, L. V. Saraf, Z. Yang, J. Liu, *Nano Lett.* **2012**, *12*, 3783.
[5] Y. S. Yun, Y.-U. Park, S.-J. Chang, B. H. Kim, J. Choi, J. Wang, D. Zhang, P. V. Braun, H.-J. Jin, K. Kang, *Carbon* **2016**, *99*, 658.
[6] D. A. Stevens, J. R. Dahn, *J. Electrochem. Soc.* **2001**, *148*, A803.
[7] D. A. Stevens, J. R. Dahn, *J. Electrochem. Soc.* **2000**, *147*, 1271.
[8] P. Thomas, D. Billaud, *Electrochim. Acta* **2002**, *47*, 3303.
[9] S. Komaba, W. Murata, T. Ishikawa, N. Yabuuchi, T. Ozeki, T. Nakayama, A. Ogata, K. Gotoh, K. Fujiwara, *Adv. Funct. Mater.* **2011**, *21*, 3859.
[10] Y. S. Yun, K.-Y. Park, B. Lee, S. Y. Cho, Y.-U. Park, S. J. Hong, B. H. Kim, H. Gwon, H. Kim, S. Lee, Y. W. Park, H.-J. Jin, K. Kang, *Adv. Mater.* **2015**, *27*, 6914.
[11] Y. S. Yun, S. Y. Cho, H. Kim, H.-J. Jin, K. Kang, *ChemElectroChem* **2015**, *2*, 359.
[12] K. Tang, L. Fu, R. J. White, L. Yu, M.-M. Titirici, M. Antonietti, J. Maier, *Adv. Energy Mater.* **2012**, *2*, 873.
[13] Z. Wang, L. Qie, L. Yuan, W. Zhang, X. Hu, Y. Huang, *Carbon* **2013**, *55*, 328.
[14] Y.-X. Wang, S.-L. Chou, H.-K. Liu, S.-X. Dou, *Carbon* **2013**, *57*, 202.
[15] Y. Liu, N. Zhang, L. Jiao, Z. Tao, J. Chen, *Adv. Funct. Mater.* **2015**, *25*, 214.
[16] Y. Xu, Y. Zhu, Y. Liu, C. Wang, *Adv. Energy Mater.* **2013**, *3*, 128.
[17] Y. Zhu, X. Han, Y. Xu, Y. Liu, S. Zheng, K. Xu, L. Hu, C. Wang, *ACS Nano* **2013**, *7*, 6378.
[18] L. Wu, X. Hu, J. Qian, F. Pei, F. Wu, R. Mao, X. Ai, H. Yang, Y. Cao, *Energy Environ.* **2014**, *7*, 323.
[19] A. Darwiche, R. Dugas, B. Fraisse, L. Monconduit, *J. Power Sources* **2016**, *304*, 1.
[20] B. Farbod, K. Cui, W. P. Kalisvaart, M. Kupsta, B. Zahiri, A. Kohandehghan, E. M. Lotfabad, Z. Li, E. J. Luber, D. Mitlin, *ACS Nano* **2014**, *8*, 4415.
[21] D. Su, H.-J. Ahn, G. Wang, *Chem. Commun.* **2013**, *49*, 3131.
[22] Y. Jiang, M. Hu, D. Zhang, T. Yuan, W. Sun, B. Xu, M. Yan, *ACS Energy* **2014**, *5*, 60.
[23] D. Y. W. Yu, P. V. Prikhodchenko, C. W. Mason, S. K. Batabyal, J. Gun, S. Sladkevich, A. G. Medvedev, O. Lev, *Nat. Commun.* **2013**, *4*, 2922.
[24] B. Qu, C. Ma, G. Ji, C. Xu, J. Xu, Y. S. Meng, T. Wang, J. Y. Lee, *Adv. Mater.* **2014**, *26*, 3854.
[25] L. Wu, X. Hu, J. Qian, F. Pei, F. Wu, R. Mao, X. Ai, H. Yang, Y. Cao, *J. Mater. Chem.* **2013**, *1*, 7181.
[26] W. Li, S.-L. Chou, J.-Z. Wang, J. H. Kim, H.-K. Liu, S.-X. Dou, *Adv. Mater.* **2014**, *26*, 4037.
[27] Y. Kim, Y. Kim, A. Choi, S. Woo, D. Mok, N.-S. Choi, Y. S. Jung, J. H. Ryu, S. M. Oh, K. T. Lee, *Adv. Mater.* **2014**, *26*, 4139.
[28] Y. Park, D.-S. Shin, S. H. Woo, N. S. Choi, K. H. Shin, S. M. Oh, K. T. Lee, S. Y. Hong, *Adv. Mater.* **2012**, *24*, 3562.
[29] Z. Zhu, H. Li, J. Liang, Z. Tao, J. Chen, *Chem. Commun.* **2015**, *51*, 1446.
[30] S. Wang, L. Wang, Z. Zhu, Z. Hu, Q. Zhao, J. Chen, *Angew. Chem. Int. Ed.* **2014**, *53*, 5892.
[31] T. Zhou, W. P. Pang, C. Zhang, J. Yang, Z. Chen, H. K. Liu, Z. Guo, *ACS Nano* **2014**, *8*, 8323.
[32] Y. C. Lu, C. Ma, J. Alvarado, N. Dimov, Y. S. Meng, S. Okada, *J. Mater. Chem. A* **2015**, *3*, 16971.
[33] C. Zhu, P. Kopold, W. Li, P. V. van Aken, J. Maier, Y. A. Yu, *Adv. Sci.* **2015**, *2*, 1500200.
[34] V. L. Chevrier, G. Ceder, *J. Electrochem. Soc.* **2011**, *158*, A1011.
[35] F. Tu, X. Xu, P. Wang, L. Si, X. Zhou, J. Bao, *J. Phys. Chem. C* **2017**, *121*, 3261.
[36] X. Zhou, L. Yu, X. W. Lou, *Adv. Energy Mater.* **2016**, *6*, 1600451.
[37] X. Zhou, L. Yu, X.-Y. Yu, X. W. Lou, *Adv. Energy Mater.* **2016**, *6*, 1601177.
[38] X. Zhou, L. Yu, X. W. Lou, *Nanoscale* **2016**, *8*, 8384.
[39] E. C. Greyson, J. E. Barton, T. W. Odom, *Small* **2006**, *2*, 368.
[40] J. W. Wang, X. H. Liu, S. X. Mao, J. Y. Huang, *Nano Lett.* **2012**, *12*, 5897.
[41] Y.-U. Park, D.-H. Seo, H.-S. Kwon, B. Kim, J. Kim, H. Kim, I. Kim, H.-I. Yoo, K. Kang, *J. Am. Chem. Soc.* **2013**, *135*, 13870.
[42] H. Song, L. Shen, J. Wang, C. Wang, *J. Mater. Chem. A* **2016**, *4*, 15411.
[43] N. Xu, X. Ma, M. Wang, T. Qian, J. Liang, W. Yang, Y. Wang, J. Hu, C. Yan, *Electrochim. Acta* **2016**, *203*, 171.
[44] L. Liang, Y. Xu, C. Wang, L. Wen, Y. Fang, Y. Mi, M. Zhou, H. Zhao, Y. Lei, *Energy Environ.* **2015**, *8*, 2954.
[45] N. Wang, Z. Bai, Y. Qian, J. Yang, *Adv. Mater.* **2016**, *28*, 4126.
[46] F. Wan, J.-Z. Guo, X.-H. Zhang, J.-P. Zhang, H.-Z. Sun, Q. Yan, D.-X. Han, L. Niu, X.-L. Wu, *ACS Appl. Mater. Interfaces* **2016**, *8*, 7790.

Received: March 8, 2017
Revised: April 24, 2017
Published online: June 12, 2017

